En face parametric imaging of tissue birefringence using polarization-sensitive optical coherence tomography

Lixin Chin
Xiaojie Yang
Robert A. McLaughlin
Peter B. Noble
David D. Sampson

En face parametric imaging of tissue birefringence using polarization-sensitive optical coherence tomography

Lixin Chin,^a Xiaojie Yang,^a Robert A. McLaughlin,^a Peter B. Noble,^{b,c} and David D. Sampson^{a,d}

[a]The University of Western Australia, School of Electrical, Electronic and Computer Engineering, Optical + Biomedical Engineering Laboratory, M018, 35 Stirling Highway, Crawley, Western Australia 6009, Australia
[b]The University of Western Australia, School of Anatomy, Physiology and Human Biology, M309, 35 Stirling Highway, Crawley, Western Australia 6009, Australia
[c]The University of Western Australia, School of Paediatrics and Child Health, Centre for Neonatal Research and Education, M550, 35 Stirling Highway, Crawley, Western Australia 6009, Australia
[d]The University of Western Australia, Centre for Microscopy, Characterisation and Analysis, M018, 35 Stirling Highway, Crawley, Western Australia 6009, Australia

Abstract. A technique for generating *en face* parametric images of tissue birefringence from scans acquired using a fiber-based polarization-sensitive optical coherence tomography (PS-OCT) system utilizing only a single-incident polarization state is presented. The value of birefringence is calculated for each A-scan in the PS-OCT volume using a quadrature demodulation and phase unwrapping algorithm. The algorithm additionally uses weighted spatial averaging and weighted least squares regression to account for the variation in phase accuracies due to varying OCT signal-to-noise-ratio. The utility of this technique is demonstrated using a model of thermally induced damage in porcine tendon and validated against histology. The resulting *en face* images of tissue birefringence are more useful than conventional PS-OCT B-scans in assessing the severity of tissue damage and in localizing the spatial extent of damage. © *2013 Society of Photo-Optical Instrumentation Engineers (SPIE)* [DOI: 10.1117/1.JBO.18.6.066005]

1 Introduction

Many types of tissue exhibit birefringence, such as those of the musculoskeletal system—muscle, cartilage, ligaments, and tendon.[1,2] Birefringence in biological tissue results from the presence and arrangement of anisotropic ultrastructures. Disease and other processes can disrupt these structures and reduce the degree of birefringence. Quantification of birefringence is, thus, a potential metric for quantifying tissue damage.[1,2] The shape, extent, and distribution of the damaged regions are also informative in pathological assessment, and an *en face* view of birefringence could provide additional spatial information about the damaged tissue.

Polarization-sensitive optical coherence tomography (PS-OCT) is a noninvasive imaging modality that can quantify the birefringence in tissue by measuring the changes in the polarization of backscattered light.[3] Local estimates of birefringence are calculated from PS-OCT scans using the rate of change of phase retardation with axial depth.[4] Computing this parameter for each A-scan in the volume generates a two-dimensional (2-D) map of birefringence. We refer to this map as a parametric image,[5] where the pixel intensity at each (*x, y*) location is indicative of an optical parameter, birefringence, calculated from the underlying PS-OCT data. Such an image gives a visual representation of the changes in birefringence, and hence the extent of tissue damage.

Sakai et al. presented a method for generating parametric images of birefringence from PS-OCT scans of human skin.[6]

However, skin possesses relatively low levels of birefringence, ≈10% of the birefringence of tendon or 20% of that of skeletal muscle.[1,6–8] Highly birefringent tissue presents the additional complication of phase wrapping.[9]

One method of overcoming the problem of phase wrapping is to calculate the local phase retardation from cumulative Jones matrix measurements. This requires calculating the local change in the tissue's optical axis, which in fiber-based PS-OCT systems is typically accomplished by sampling the tissue using multiple incident polarization states.[9,10] Alternatively, Stifter et al. adopted a signal processing technique to unwrap the cumulative phase retardation based on a 2-D quadrature transformation.[11] They demonstrated its use in imaging the cross-sectional (B-scan) view of the birefringence of polymer materials under stress.[11] However, the accuracy of the phase retardation signal is related to the signal-to-noise ratio (SNR) of the OCT signal (OCT SNR).[4,12] Previously reported methods have not accounted for this reduction in accuracy in areas of low signal, such as in the troughs of OCT speckle, or with increasing depth into the tissue.

We propose a fully automated signal processing algorithm to quantify the birefringence of a sample accounting for differing phase accuracies due to varying OCT SNR and utilizing a quadrature transformation to account for highly birefringent materials. In addition, we extend the algorithm to generate an *en face* parametric OCT image of birefringence capable of highlighting areas of tissue damage in biological samples. This method is usable on scan volumes acquired with fiber-based PS-OCT systems possessing only a single incident polarization state. The algorithm is demonstrated on porcine tendon; the degree of

Address all correspondence to: Lixin Chin, The University of Western Australia, School of Electrical, Electronic and Computer Engineering, Optical + Biomedical Engineering Laboratory, M018, 35 Stirling Highway, Crawley, Western Australia 6009, Australia. Tel: +61-8-6488-2317; Fax: +61-8-6488-1319; E-mail: chinl01@student.uwa.edu.au

measured birefringence is compared to the degree of thermally induced tissue damage, and validated against colocated histological sections.

2 Method

Generating parametric images of birefringence from PS-OCT scan volumes requires separating the value of birefringence from the other polarization altering properties of both the tissue and the PS-OCT system itself. The recorded signal from each voxel in the scan volume can be expressed as a real-valued Stokes vector, $\mathbf{S} = [I, Q, U, V]^T$, which describes the polarization state of light.[13,14] PS-OCT detects a fully polarized signal, so the Q, U, and V components fully describe the polarization state. The normalized, reduced Stokes vector (hereafter, "Stokes vector"), $\hat{\mathbf{S}} = [\hat{Q}, \hat{U}, \hat{V}]^T$, is obtained by dividing the Q, U, and V components by $I = (Q^2 + U^2 + V^2)^{1/2}$. It is common to treat the polarization changes due to the PS-OCT system as both lossless and constant during imaging.[4] The birefringence of the tissue sample can, thus, be extracted from the relative difference between Stokes vectors in an A-scan.

The phase retardation, or phase angle $\phi_r(z_i)$, is the angle between the Stokes vectors $\hat{\mathbf{S}}_{ref}$ (at the surface of the tissue) and $\hat{\mathbf{S}}(z_i)$ (at a depth z_i into the tissue). That is, $\cos[\phi_r(z_i)] = \hat{\mathbf{S}}_{ref} \bullet \hat{\mathbf{S}}(z_i)$, where $\bullet$ is the three-dimensional (3-D) vector dot product and the subscript i represents the discretization of the OCT signal in the z-dimension. The measurement accuracy of $\phi_r(z_i)$ is affected by the OCT SNR, which varies due to speckle, and decreases with depth into the tissue. In the shot-noise limit, noise can be modeled as a circularly symmetric complex Gaussian random variable [zero mean, phase uniformly distributed over $(-\pi, \pi)$] added to the complex electric field describing light backscattered from the sample. With high OCT SNR, this gives the variance of $\phi_r(z_i)$ as approximately twice the inverse OCT SNR at z_i, $\sigma_r^2(z_i) \approx 2/\text{SNR}(z_i)$.[4,12] The effects of varying OCT SNR due to speckle can be decreased by averaging the Stokes vectors over distances larger than the coherence length of the source.[14–16] The relationship between OCT SNR and the accuracy of $\phi_r(z_i)$ implies that the Stokes vectors should be weighted by $w(z_i) = 1/\sigma_r^2(z_i) = \text{SNR}(z_i)/2$ during spatial averaging. The variance of the angle calculated from the weighted, spatially averaged Stokes vectors is then given by $\sigma_{av}^2 = 2/(K \otimes \text{SNR}) = 2/\text{SNR}_{av}$, where $\otimes$ denotes the convolution operation, K the kernel used for spatial averaging, and $\text{SNR}_{av} = K \otimes \text{SNR}$ the "spatially averaged" SNR.

In a noise-free model, the angle, $\phi_r(z_i)$, between Stokes vectors is a function of the polarization state of light incident on the tissue (hereafter "incident polarization"), the diattenuation of the tissue, the birefringence of the tissue, and the orientation of the tissue's optical axis.[16] If the tissue's optical axis changes minimally within an A-scan, its effects on $\phi_r(z_i)$ will be limited and can be modeled as a low-frequency modulation allowing $\phi_r(z_i)$ to be measured using a single-incident polarization state. The incident polarization should ideally be circular or linearly polarized at 45 deg to the tissue optical axis. Misalignment of the incident polarization away from these target polarization states degrades the effective SNR of $\phi_r(z_i)$.[16]

The effects of incident polarization, diattenuation, and changing optical axis with depth into the tissue can be modeled as modulations of the amplitude, $A(z_i)$, of the cosine-phase signal with depth,[11,16]

$$\hat{\mathbf{S}}_{ref} \bullet \hat{\mathbf{S}}(z_i) = C_{in}(z_i) = A(z_i) \cos[\phi_c(z_i)]. \quad (1)$$

This leaves $\phi_c(z_i)$, the continuous-phase retardation with depth, as a function of tissue birefringence. The amplitude modulations, $A(z_i)$, can be removed using the quadrature component, $C_{quad}(z_i) = A(z_i) \sin[\phi_c(z_i)]$, determined using the Hilbert transform, H, to the in-phase signal $C_{in}(z_i)$. That is, $C_{quad}(z_i) = H(C_{in})(z_i)$.[11] This gives the demodulated, wrapped, phase retardation,

$$\phi_w(z_i) = \angle[C_{in}(z_i) + iC_{quad}(z_i)]. \quad (2)$$

As $\phi_w(z_i)$ is discretized in z_i, it can be unwrapped by considering the difference between successive values, $\phi_{diff}(z_i) = \phi_w(z_i) - \phi_w(z_{i-1})$. Phase wrapping is considered to occur at the values of z_i for which $|\phi_{diff}(z_i)|$ exceeds a threshold, and phase unwrapping is performed by interpolating $\phi_{diff}(z_i)$ at these locations. Calculating the cumulative sum of $\phi_{diff}(z_i)$ with depth gives the unwrapped double-pass phase retardation $\phi_u(z_i) = \sum_{j=0}^{i} \phi_{diff}(z_j)$. The birefringence, Δn, in each A-scan is then calculated as
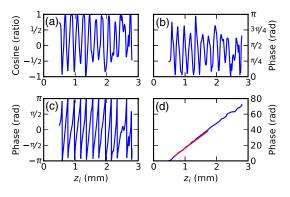
$$\Delta n = \text{RI} \times \delta\phi_u \times \lambda_0/(4\pi), \quad (3)$$

where RI is the bulk refractive index of the tissue sample, λ_0 is the mean wavelength of the PS-OCT system, and $\delta\phi_u$ is the slope of $\phi_u(z_i)$.[14] The slope of the phase retardation with depth, $\delta\phi_u$, is obtained using weighted least squares linear regression, with the weight at each point equal to half of the spatially averaged OCT SNR at that point ($\text{SNR}_{av}/2$). Figure 1 shows this process on a single representative A-scan.

3 Experiment

3.1 PS-OCT Imaging

The algorithm described here was applied to scans acquired using a fiber-based, swept-source PS-OCT system (PSOCT-1300, Thorlabs, New Jersey).[17] This system has a manufacturer specified mean wavelength/spectral bandwidth of 1325 nm/ 100 nm and a measured axial/lateral resolution of 17 µm/ 16 µm in air [full-width-at-half-maximum (FWHM) of intensity]. The incident polarization was manually adjusted before scanning to maximize the SNR of the phase retardation signal. Scan volumes were acquired measuring $4 \times 4 \times 2.8$ mm

Fig. 1 Quadrature demodulation and phase unwrapping applied to a single representative A-scan. Using the angle between the weighted, spatially averaged Stokes vectors [shown as (a) $\cos[\phi_r(z_i)]$ and (b) $\phi_r(z_i)$], (c) is the wrapped, double-pass, demodulated phase retardation, $\phi_w(z_i)$, and (d) is the unwrapped, double-pass, demodulated phase retardation, $\phi_u(z_i)$, along with a linear fit (in red) over a 300 µm range (length exaggerated for visibility).

$(832 \times 832 \times 512$ pixels). The Stokes vectors within each B-scan were spatially averaged using a 2-D Gaussian kernel with FWHM in z/x equal to twice the OCT axial/lateral resolution. After demodulation using the Hilbert transform, $\phi_w(z_i)$ was unwrapped using a threshold on $|\phi_{\text{diff}}(z_i)|$ of 0.5 rad/pixel (≈ 0.091 rad/μm). The slope of $\phi_u(z_i)$ was calculated using weighted least squares regression over a range of 300 μm, starting approximately at 175 μm from the surface of the tissue, and the *en face* parametric image of tissue birefringence was calculated using Eq. (3) for each A-scan.
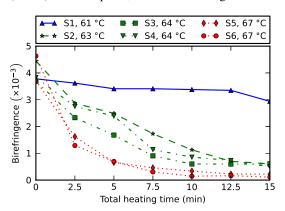
3.2 *Thermally Damaged Porcine Tendon*

Scans were acquired of porcine tendon that had its birefringence decreased through thermal stress. Fresh tendon is highly birefringent; however, once heated above an activation temperature (≈ 62°C for these samples), the collagen in the tendon denatures. This leads to a decrease in birefringence with the rate of decrease being a function of both temperature and heating time.[2,8] This model was used both to quantify birefringence and to generate *en face* parametric OCT images of birefringence.

Three castrated-male pigs (≈ 8 to 10 weeks, 30 kg) were euthanized by exsanguination under barbiturate anesthesia in accordance with institutional ethics requirements. Tendons were extracted from the posterior side of the hind limbs, and cut into strips measuring approximately $10 \times 10 \times 5$ mm. The samples were clamped between aluminum blocks and fully immersed in heated physiological Krebs solution. After 2.5 min, the samples were removed from solution and imaged on the PS-OCT system. The samples were then replaced in the heated Krebs solution for a further 2.5 min, and the process repeated until each sample had been heated for a total of 15 min. *En face* parametric birefringence images of each sample were generated using the described algorithm, taking the bulk refractive index of porcine tendon, RI, as 1.4.[8,18]

4 Results

Figure 2 shows the mean birefringence for six tendon samples at temperatures ranging from 61°C to 67°C. The birefringence of fresh tendon prior to thermal stress ($t = 0$ min) was $4.0 \times 10^{-3} \pm 0.4 \times 10^{-3}$ (mean $\pm$ standard deviation), comparable with previously reported values of $4.2 \times 10^{-3} \pm 0.3 \times 10^{-3}$ (Ref. 8). As anticipated, the mean birefringence decreased

with time, as the period of thermal stress increased, and the rate at which the birefringence decreased was observed to increase with temperature. Tendon birefringence was generally unchanged by heating at 61°C, but had mostly dissipated after 7.5 min at 67°C. This agrees with previous studies, which showed that porcine tendon was unaffected by heating at 60°C, but rapidly denatured at 65°C.[19]

Additionally, one tendon was cut to 2 cm in length and suspended such that one end was immersed in heated Krebs solution (69°C for 5 min), while the other end was left in air (≈ 60°C). PS-OCT scans were acquired both before and after heating. The sample was then fixed in formaldehyde, embedded in paraffin wax, sectioned, and stained with haematoxylin and eosin (H&E). Figure 3 shows three phase-retardation B-scans from regions of the sample after heating. Figure 4 shows the *en face* parametric images of the sample birefringence before and after heating, and the corresponding histological section and OCT intensity images.

The mean birefringence of the sample prior to heating was 4.5×10^{-3}, which is within the expected range. After heating, there is a visible difference in the phase retardation B-scans from the immersed region [Fig. 3(a)] compared to the nonimmersed region [Fig. 3(c)], although the boundary between the two regions is more difficult to discern in the B-scan [Fig. 3(b)]. By contrast, the *en face* parametric image shows a clear boundary between the low- and high-birefringence regions [Fig. 4(d)], corresponding to the liquid–air interface during the heating protocol. The boundary in the parametric image is also more apparent than in the corresponding *en face* OCT intensity image [Fig. 4(c)]. The mean birefringence after heating was 6.1×10^{-4} in the immersed region and 3.2×10^{-3} in the nonimmersed region. This is comparable with the mean birefringence after 5 min of the samples heated to 67°C (6.8×10^{-4}) and 61°C (3.4×10^{-3}), respectively. The liquid–air boundary is also evident in the histological section [Fig. 4(e)]. The damaged region stains a deep purple, and the collagen weave has lost its fine structure and fused together. The large tears are artifacts resulting from the weakened tissue breaking during histological processing. There is a clear correspondence between the *en face* parametric image of tissue birefringence [Fig. 4(d)] and the colocated H&E stained histological section [Fig. 4(e)].

5 Discussion

Results presented here demonstrate the ability of an *en face* parametric OCT image of birefringence to improve differentiation of tissue damage. Compared to the B-scan images of phase retardation (Fig. 3), the *en face* parametric images of birefringence (Fig. 4) show a clearer view of the lateral extent of the tissue damage as well as presenting the same orientation as conventional polarized light microscopy. We note that the parametric OCT image of birefringence has compressed the 3-D PS-OCT volume into a more concise 2-D representation showing areas of tissue damage.

This study used an empirically chosen range of 300 μm over which to calculate tissue birefringence. From Eq. (3), the precision of the calculated birefringence is proportional to the precision of the slope of the phase retardation with depth. The standard deviation of the slope of the phase retardation can be modeled as the standard deviation of the slope parameter of a weighted least squares linear estimator.[20] Using a single-scattering model of OCT, taking the attenuation coefficient of tendon as 0.24 mm^{-1} (Ref. 21), and an initial OCT SNR of 30 dB, the

Fig. 2 The mean birefringence of porcine tendon samples (S1 to S6) after thermal stress. Samples were immersed in heated Krebs solution at the indicated temperatures; 61°C (blue), 63°C to 64°C (green), and 67°C (red). Total heating time refers to the duration of the applied thermal stress.
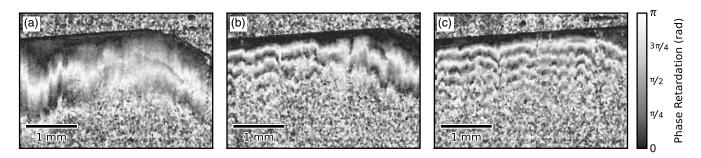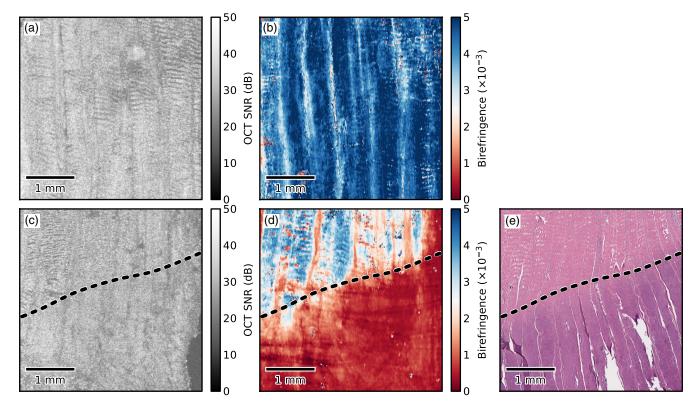
Fig. 3 Phase retardation B-scans of a porcine tendon sample after partial immersion into 69°C Krebs solution for 5 min. (a) From a section of the sample which was immersed into solution. (b) From the boundary between the immersed (right) and nonimmersed (left) regions. (c) From the nonimmersed region.

Fig. 4 *En face* optical coherence tomography (OCT) intensity images of the same porcine tendon sample depicted in Fig. 3, (a) before and (c) after partial immersion into 69°C Krebs solution for 5 min. (b, d) Corresponding *en face* parametric OCT images of tissue birefringence. (e) Haematoxylin and eosin (H&E) stained histological section corresponding to the region shown in (c) and (d). The dashed lines indicate the location of the liquid–air boundary during heating.

300 μm fitting range corresponds to an estimated standard deviation on the slope of the phase retardation of 0.072 rad/mm, leading to a standard deviation on the birefringence estimate of 1.1×10^{-5}. Halving this range to 150 μm would increase the standard deviation of the birefringence estimates by a factor of ≈ 3. Similarly, doubling the range to 600 μm would decrease this standard deviation by a factor of ≈ 3. However, increasing the fitting range also increases the possibility of errors due to aggregating birefringence over different tissue types. The optimal fitting length will be application specific, depending on the anticipated homogeneity of the tissue.

The current implementation assumes tissue homogeneity within the section of the A-scan used to calculate the birefringence. This is likely to be the case when imaging musculoskeletal tissue such as tendon or muscle, which consist mostly of a single tissue type, but may not be the case in complex biological structures such as airways. In this situation, a segmentation algorithm (e.g., as shown by van Soest et al.[22]) will be necessary to identify homogenous regions of tissue, so that the birefringence of each tissue type can be calculated separately.

The presented method has been demonstrated on *ex vivo* tissue samples. The low penetration depth of PS-OCT (≈ 1 to 2 mm in tissue) presents a challenge to extending this work to *in vivo* imaging. In addition, the method works best if the incident polarization state is manually optimized before imaging, but such adjustments also complicate the potential *in vivo* imaging scenarios. To overcome the challenge posed by the low penetration depth of OCT-based imaging modalities, several groups have shown that OCT imaging probes can be miniaturized and encased within hypodermic needles[23–26] and endoscopes.[22,27–29] OCT needle probes capable of acquiring 3-D scans have been reported to be as small as 30-gauge (outer

diameter 310 μm),[24,30] significantly smaller than standard biopsy needles. PS-OCT needle probes could be used interstitially to image birefringent tissues such as tendon, muscle, or cartilage *in situ*. OCT endoscopic probes have been demonstrated capable of *in vivo* imaging of human airways[27] and arteries,[22] and PS-OCT endoscopic probes have been demonstrated on *ex vivo* human arteries.[28] Additionally, as one method of addressing the challenge posed by the optimization of the incident polarization state, it has been shown that fiber-based PS-OCT systems may be constructed using polarization-maintaining fibers (PMFs).[31,32] PMF-based systems keep the use of a single incident polarization state, but do not require tuning of the incident polarization before each scan.[31] In combination with the techniques presented, PS-OCT needle and endoscopic probes and PMF-based PS-OCT systems could enable the generation of parametric OCT images of tissue birefringence *in vivo*.

6 Conclusion

In summary, we have demonstrated an automated method to quantify birefringence in PS-OCT volumes and have used this to define a novel *en face* parametric image. This method accounts for variances in phase accuracy due to differing OCT SNR, improving performance compared to conventional mean filtering, and accounts for highly birefringent tissue by utilizing quadrature demodulation and phase unwrapping. In addition, this method is useable with fiber-based PS-OCT systems possessing only a single-incident polarization state. When compared against OCT, the *en face* parametric image of birefringence gave clear visualization of the damage in birefringent tissue and enabled automated quantification of the degree of tissue damage.

References

1. M. S. Islam et al., "Extracting structural features of rat sciatic nerve using polarization-sensitive spectral domain optical coherence tomography," *J. Biomed. Opt.* **17**(5), 056012 (2012).
2. D. J. Maitland and J. T. Walsh Jr., "Quantitative measurements of linear birefringence during heating of native collagen," *Lasers Surg. Med.* **20**(3), 310–318 (1997).
3. J. F. de Boer et al., "Two-dimensional birefringence imaging in biological tissue by polarization-sensitive optical coherence tomography," *Opt. Lett.* **22**(12), 934–936 (1997).
4. B. H. Park et al., "Real-time fiber-based multi-functional spectral-domain optical coherence tomography at 1.3 μm," *Opt. Express* **13**(11), 3931–3944 (2005).
5. R. A. McLaughlin et al., "Parametric imaging of cancer with optical coherence tomography," *J. Biomed. Opt.* **15**(4), 046029 (2010).
6. S. Sakai et al., "Relationship between dermal birefringence and the skin surface roughness of photoaged human skin," *J. Biomed. Opt.* **14**(4), 044032 (2009).
7. K. H. Kim et al., "*In vivo* imaging of human burn injuries with polarization-sensitive optical coherence tomography," *J. Biomed. Opt.* **17**(6), 066012 (2012).
8. S. Jiao and L. V. Wang, "Jones-matrix imaging of biological tissues with quadruple-channel optical coherence tomography," *J. Biomed. Opt.* **7**(3), 350–358 (2002).
9. C. Fan and G. Yao, "Mapping local retardance in birefringent samples using polarization sensitive optical coherence tomography," *Opt. Lett.* **37**(9), 1415–1417 (2012).
10. S. Makita, M. Yamanari, and Y. Yasuno, "Generalized Jones matrix optical coherence tomography: performance and local birefringence imaging," *Opt. Express* **18**(2), 854–876 (2010).
11. D. Stifter et al., "Dynamic optical studies in materials testing with spectral-domain polarization-sensitive optical coherence tomography," *Opt. Express* **18**(25), 25712–25725 (2010).
12. B. H. Park et al., "Optic axis determination accuracy for fiber-based polarization-sensitive optical coherence tomography," *Opt. Lett.* **30**(19), 2587–2589 (2005).
13. N. Ghosh and I. A. Vitkin, "Tissue polarimetry: concepts, challenges, applications, and outlook," *J. Biomed. Opt.* **16**(11), 110801 (2011).
14. J. F. de Boer and T. E. Milner, "Review of polarization sensitive optical coherence tomography and Stokes vector determination," *J. Biomed. Opt.* **7**(3), 359–371 (2002).
15. E. Z. Zhang and B. J. Vakoc, "Polarimetry noise in fiber-based optical coherence tomography instrumentation," *Opt. Express* **19**(18), 16830–16842 (2011).
16. N. J. Kemp et al., "High-sensitivity determination of birefringence in turbid media with enhanced polarization-sensitive optical coherence tomography," *J. Opt. Soc. Am. A* **22**(3), 552–560 (2005).
17. Y. M. Liew et al., "*In vivo* assessment of human burn scars through automated quantification of vascularity using optical coherence tomography," *J. Biomed. Opt.* **18**(6), 061213 (2013).
18. N. Ugryumova et al., "Novel optical imaging technique to determine the 3-D orientation of collagen fibers in cartilage: variable-incidence angle polarization-sensitive optical coherence tomography," *Osteoarthr. Cartilage* **17**(1), 33–42 (2009).
19. J. C. Wang et al., "The effect of uniform heating on the biomechanical properties of the intervertebral disc in a porcine model," *Spine J.* **5**(1), 64–70 (2005).
20. W. H. Press et al., *Numerical Recipes: The Art of Scientific Computing*, 3rd edn., Cambridge University Press, Cambridge, UK (2007).
21. M. Todorović et al., "Determination of local polarization properties of biological samples in the presence of diattenuation by use of Mueller optical coherence tomography," *Opt. Lett.* **29**(20), 2402–2404 (2004).
22. G. van Soest et al., "Atherosclerotic tissue characterization *in vivo* by optical coherence tomography attenuation imaging," *J. Biomed. Opt.* **15**(1), 011105 (2010).
23. L. Scolaro et al., "High-sensitivity anastigmatic imaging needle for optical coherence tomography," *Opt. Lett.* **37**(24), 5247–5249 (2012).
24. R. A. McLaughlin et al., "Static and dynamic imaging of alveoli using optical coherence tomography needle probes," *J. Appl. Physiol.* **113**(6), 967–974 (2012).
25. B. C. Quirk et al., "In situ imaging of lung alveoli with an optical coherence tomography needle probe," *J. Biomed. Opt.* **16**(3), 036009 (2011).
26. Y. Wu et al., "Robust high-resolution fine OCT needle for side-viewing interstitial tissue imaging," *IEEE J. Sel. Topics Quantum Electron.* **16**(4), 863–869 (2010).
27. J. P. Williamson et al., "Measuring airway dimensions during bronchoscopy using anatomical optical coherence tomography," *Eur. Respir. J.* **35**(1), 34–41 (2010).
28. S. D. Giattina et al., "Assessment of coronary plaque collagen with polarization sensitive optical coherence tomography (PS-OCT)," *Int. J. Cardiol.* **107**(3), 400–409 (2006).
29. P. B. Noble et al., "Airway narrowing assessed by anatomical optical coherence tomography *in vitro*: dynamic airway wall morphology and function," *J. Appl. Physiol.* **108**(2), 401–411 (2010).
30. D. Lorenser et al., "Ultrathin side-viewing needle probe for optical coherence tomography," *Opt. Lett.* **36**(19), 3894–3896 (2011).
31. E. Götzinger et al., "Polarization maintaining fiber based ultra-high resolution spectral domain polarization sensitive optical coherence tomography," *Opt. Express* **17**(25), 22704–22717 (2009).
32. M. K. Al-Qaisi and T. Akkin, "Swept-source polarization-sensitive optical coherence tomography based on polarization-maintaining fiber," *Opt. Express* **18**(4), 3392–3403 (2010).